






Determination of poloidal mode numbers of MHD modes and their radial location using a soft x-ray camera array in the Wendelstein 7-X stellarator

M B Dreval^{1,*} , C Brandt² , J Schilling² , H Thomsen² , A Beletskii^{1,3} , A Könies² and the W7-X Team^{1,4}

¹ Institute of Plasma Physics, National Science Center, Kharkov Institute of Physics and Technology, 61108 Kharkov, Ukraine

² Max-Planck-Institut für Plasmaphysik, Wendelsteinstr 1, 17491 Greifswald, Germany

³ Max-Planck-Institut für Mikrostukturphysik, Weinberg 2, 06120 Halle, Germany

E-mail: mdreval@kipt.kharkov.ua

Abstract

A forward modeling technique is developed for determining the characteristic features of observed MHD modes from the line-of-sight data of the soft x-ray (SXR) tomography diagnostics in the Wendelstein 7-X (W7-X) stellarator. In particular, forward modeling is used to evaluate the poloidal mode numbers m , radial location, poloidal rotation direction and ballooning character of the MHD modes. The poloidal mode structures have been modeled by the radially localized Gaussian-shaped emission regions rotating along the magnetic surfaces. In the present study the cases of rigid-shape emission regions and flexible emission regions are modeled. Various mode phase velocity dependences on the magnetic surface position are

simulated. The modeled phase dynamics of line-integrated oscillations and the distribution of oscillation amplitudes are compared with the experimental signals of the SXR cameras which observe the plasma at various viewing angles in the poloidal cross-section. Application of this technique enables describing of the 1–50 kHz modes. In particular, in the discharge W7X-PID 20180918.045 three identified branches with the poloidal mode numbers $m = 8$, $m = 10$ and $m = 11$ localized at $\rho \approx 0.3$ are rotating in the clockwise poloidal direction. The present paper reports the first application of the forward modeling technique to the data from the SXR diagnostics in W7-X. The high m -modes are identified by forward modeling in W7-X.

Keywords: Wendelstein 7-X, MHD modes, soft x-ray diagnostics

1. Introduction

The Wendelstein 7-X stellarator (W7-X) has been designed to be MHD stable up to $\langle \beta \rangle \sim 4\%–5\%$ volume-averaged

plasma beta [1]. In order to prove if the optimization criteria have been met, it is crucial to analyze and understand any MHD mode activity in the device. Moreover, modes might be caused by physics mechanisms beyond the MHD description and their study can thus provide a deeper insight into the processes determining the plasma stability in optimized stellarators. Furthermore, a well-diagnosed mode activity may be used for ‘MHD spectroscopy’, i.e. to obtain information about

⁴ See Klinger *et al* 2019 (<https://doi.org/10.1088/1741-4326/ab03a7>) for the W7-X team.

* Author to whom any correspondence should be addressed.

the radial location and spatial structure of observed modes, which is essential to understanding driving instabilities and underlying physics.

In W7-X plasmas quasi-harmonic oscillations in the low kHz range up to multiple 100 kHz were observed in various discharges during operational phase 1.2 by various plasma fluctuation diagnostics like magnetic probes [2], phase contrast imaging [3] and the soft x-ray (SXR) tomography system [4–6]. In the present paper we focus on the 10–50 kHz modes observed by the SXR tomography diagnostics. For this we are concentrating on the radial location and poloidal mode numbers of these modes.

The data from SXR cameras are commonly used for studying spatial structures of MHD instabilities in magnetically-confined high-temperature plasmas, in W7-X the soft x-ray multi-camera tomography system (XMCTS) has been put in operation for this purpose [4–6]. An initial study on tomographic reconstruction of MHD modes based on surrogate data and errors expected for the XMCTS diagnostic is described in [4]. The installation of the XMCTS in W7-X can be found in [5]. The detailed description of the final XMCTS system and first results with experimental data from W7-X and their tomographic inversion are presented in [6]. It consists of the 20 pinhole cameras, each equipped with a silicon diode detector array with 18 channels. This system provides excellent capabilities for studying the spatial structure of the MHD modes.

The analysis of the mode structure from the SXR raw data is not straightforward one due to the line-of-sight integral nature of the SXR signals. The mode dynamics is usually observed by the poloidal propagation (in literature mostly called as ‘rotation’) of plasma parameter perturbations. The perturbation crosses twice a line-of-sight of SXR diagnostics during a full poloidal turn. In the SXR signals the impacts of positive and negative emissivity of the mode perturbations are combined. A spectral analysis of raw SXR signals can be used to determine the radial locations of MHD modes without tomographic inversion [7–11]. The poloidal mode number and radial location can be determined using a singular value decomposition technique [7, 9]. Forward modeling [7, 12, 13] can be used for this purpose as well. It can also reveal a detailed mode structure while the tomography method yields an unstable or spurious image. In particular, as is known, the modes are localized from other diagnostics or other knowledge, forward modeling can reveal finer structures than tomography.

2. Models and features of forward modeling techniques

The SXR forward modeling technique is based on a comparison of experimental data with the line-integration of a synthetic emissivity. In contrast to the usual tomography, the direct problem is solved in the forward modeling approach. Additional constraints implemented in forward modeling can substantially increase the diagnostic resolution, simplify and speed-up the subroutines in comparison with the conventional

tomography. These constraints can be adapted according to the goal of the modeling.

We are studying the fluctuations of SXR emission caused by plasma modes. The constant background SXR radiation part is out of scope of our modeling. The background part of the SXR emission is subtracted from the experimental data and is not considered in the model. The fluctuating plasma density inside the plasma mode causes positive and negative perturbations of the SXR emissivity in relation to the SXR background emissivity. For forward modeling of the plasma modes in the context of our study a synthetic perturbation pattern is applied. The approach of using mode eigenfunctions can be used in forward modeling of line-integrated diagnostics such as SXR or phase contrast imaging diagnostics [14]. However these eigenfunctions are usually not known, if the mode type is unknown. Constraints in this case are based on the nature of typical MHD modes in stellarators. Most of the MHD modes in stellarators and tokamaks are localized on the magnetic flux surfaces. This fact is used as constraints in the models.

The dependence of the mode rotation velocity on the poloidal angle should be implemented in the model as the next step. The perturbation rotation velocity is equivalent to the phase velocity of the mode. A rotation of the centers of the perturbations can be expressed by: $A(l, t) = A_0 \sin(kl - \omega t) = A_0 \sin(\Phi)$, where A_0 is the mode amplitude, l is the poloidal position of the perturbation in the magnetic flux surface, k is the wavevector, ω is the angular frequency, t is the time. The phase velocity is the velocity of the constant phase Φ . From $d\Phi/dt = 0$ we can obtain the phase velocity formula: $v_\Phi = \omega / (k + l \cdot dk/dl)$ in the case of constant ω . The phase velocity dependence on the poloidal angle $v_\Phi(l(\theta))$ is contained in the $(k + l \cdot dk/dl)^{-1}$ term. Thus, the angular dependence of the perturbation velocity can be modeled via the direct determination of the phase velocity $v_\Phi(\theta)$ or via the determination of the wavevector dependence $k(l(\theta))$. One of these two equivalent (for the constant ω) approaches can be selected in a particular case. For example, the shear Alfvén eigenmodes [15] are formed by coupling of two counterpropagating waves. The coupling of m and $m + 1$ continuum modes causes the toroidicity induced Alfvén eigenmode (TAE) formation. The coupling of the m and $m + 1$ modes in the oversimplified case can be described as: $\cos(m\theta - \omega t) + \cos(-(m + 1)\theta - \omega t) \sim \cos(\theta/2)$. Thus, the ballooning TAE mode is located mainly at the low field side where $-\pi/2 < \theta < \pi/2$. This mode can be modeled via the angular dependence of the combined mode wavevector in order to highlight the ballooning nature represented by the $\cos(\theta/2)$ term. This case can be modeled via the direct determination of phase velocities of m and $m + 1$ modes.

A dependence of the wavevector on the magnetic surface position causes deformation of the perturbation shape. This shape can be modeled by the eigenfunctions of the mode, if this information is available. The set of rigid rotating Gaussian perturbations can be used as a first approach in the opposite case. The angular dependence of the wavevector results in perturbation deformations. This can be taken into account in more sophisticated models. The perturbation length λ along the

magnetic flux surface increases with phase velocity increasing ($v_{\Phi} \approx \omega/k \sim \lambda$). The perturbation size in the perpendicular direction should be inversely proportional to the length along the flux surface due to the integrated perturbation amplitude conservation. This also should depend on the angular variable distance between the neighboring flux surfaces.

Various criteria of a comparison of the experimental data with the line-integration of the synthetic emissivity can be selected. In the first approach the influence of the spatial mode structure on the line-integrated signals can be analyzed. For example, in the oversimplified ballooning TAE case the term $\cos(\theta/2)$ indicates that the mode should be observed mainly in the low field side of a tokamak. One more criterion is based on the comparison of oscillation amplitudes in the different SXR lines-of-sight. The techniques based on the spatial modes structure use this criterion. These based on the mode amplitude (or amplitude and phase) distribution techniques are considered in ASDEX-U [9, 10] for low frequency and low- m kink and tearing modes or high frequency low- m reversed shear Alfvén eigenmode modes in Alcator C-Mod [14].

A more improved comparison is based on the phase dynamics of line-integrated oscillations. This phase dynamics caused by the spatiotemporal mode evolution accumulates the contributions of the spatiotemporal evolution of each mode perturbation. The techniques based on the spatiotemporal approach are used for low frequency and low- m modes in RFP [11] and STOR-M [13] for low frequency and average- m modes in W7-AS [7] and U-3M [12].

The perturbations cross the line-of-sight twice during a full poloidal turn along the flux surface. The line-integration of the opposite propagating mode perturbations leads to the interference that causes rather complex phase diagrams. The phase diagram is reconstructed on the base of synthetic perturbations in the real geometry of the SXR diagnostics. This diagram is used as an advanced criterion in forward modeling. It contains information about the mode structure encrypted by the line-integration. For example, a divergence of the lines-of-sight causes a different apparent velocity of the perturbation in the near and far parts of the flux surface with respect to the camera. On the base of this difference it is possible to evaluate the mode rotation direction [13]. The asymmetry of the flux surfaces can be used for determination of this direction too [12]. In the present work, we first describe the experimental determination of the radial location, poloidal mode numbers and direction of 10–50 kHz modes poloidal rotation in the W7-X stellarator by applying the forward modeling approach.

3. SXR system and experimentally observed oscillations

Figure 1 shows the lines-of-sight of the three SXR pin-hole cameras plotted across the magnetic flux surfaces calculated by the VMEC equilibrium code [16]. The cameras with labels ‘1B’, ‘1D’ and ‘1E’ are chosen from the 20 available XMCTS cameras for covering different viewing angles sufficient for the signal processing technique. The view cones of the central line-of-sight span a poloidal angle of

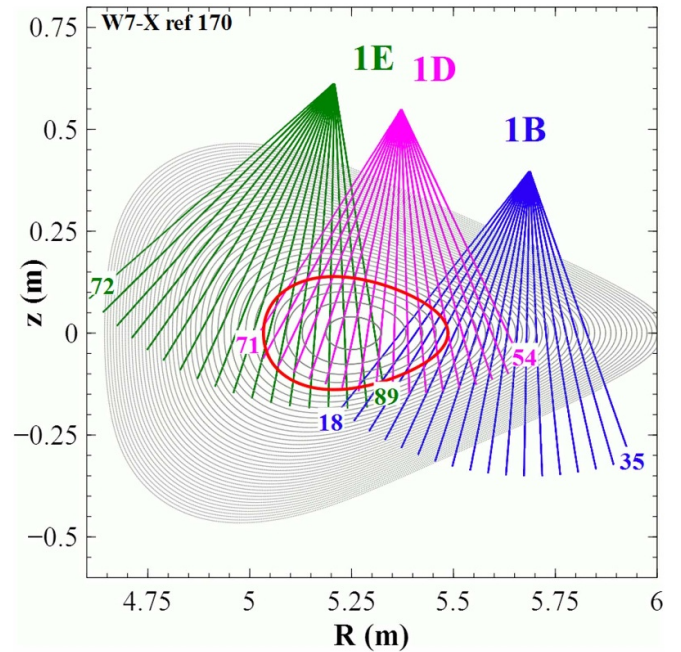


Figure 1. Lines-of-sight of SXR cameras 1B, 1D and 1E across the W7-X flux surfaces of the magnetic configuration W7-X ref 170. The red flux surface at $\rho \equiv r/r_{\text{LCFS}} \approx 0.3$ corresponds to the mode location under consideration whereas r_{LCFS} represents the last closed flux surface.

3.7°. A discharge (W7X-PID 20180918.045) with transient 20–35 kHz oscillations is depicted in figure 2(a). This spectrogram represents oscillations measured by the SXR channel #18 of camera 1B. Similar spectrograms are observed in neighboring SXR lines-of-sight. Two frequency ranges, i.e. 29–37 kHz and 23–28 kHz, can be distinguished. The oscillation amplitude dynamics of these two parts can be represented by the time evolution of root mean square (rms) of the filtered SXR signal amplitudes. The rms represents the harmonic mode amplitude. Two bandpass filters are applied to the raw SXR data in order to separate the frequency ranges under consideration. The temporal evolution of the two frequency bands observed by the photodiodes of camera 1D are plotted in figures 2(b) and (c).

Note that within the narrow frequency range of 29–37 kHz the different branches can be observed (figures 2(a) and (b)). At 3.415 s of figure 2(b) a separation of the branch with a decreasing frequency and a branch with a frequency constant in time can be distinguished.

A distinct pattern of the rms amplitude across the photodiodes can be recognized in figures 2(b) and (c). The spatial pattern of the rms amplitudes can be explained by the interference of negative and positive parts of a single (or more) plasma mode(s) aligned with the magnetic flux surfaces as detected along the lines-of-sight of the SXR camera. This effect is described in detail in the next sections. The spatial structure of the single frequency branches is quasi-stationary. This indicates that the signal-to-noise ratio of the SXR diagnostics is sufficient for the mode analysis. The phase evolution of oscillations provides more detailed information about

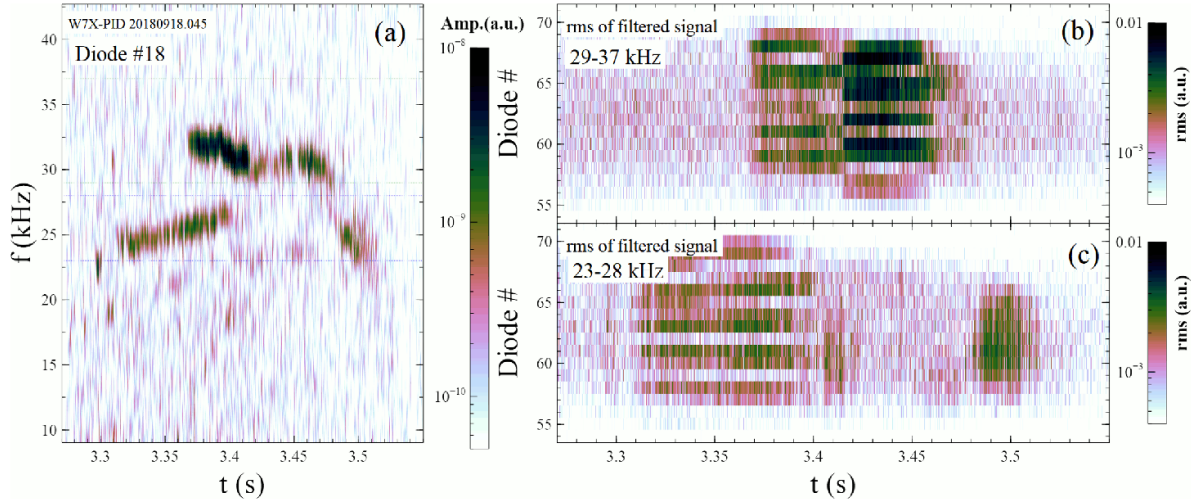


Figure 2. (a) Spectrum of SXR signal fluctuations of diode #18 (camera 1B), (b) rms of 29–37 kHz and (c) 23–28 kHz fluctuations (color coded) versus time and photodiode number of the data from the SXR camera 1D.

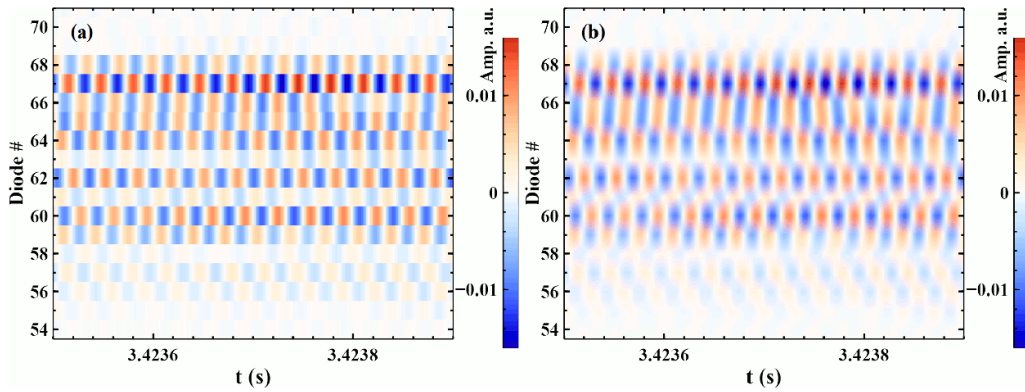


Figure 3. Spatiotemporal evolution of the SXR emission data of experimental program XP20 180 918.045, time range 400 μ s at 3.4237 s, measured by the camera 1D. A 29–37 kHz band-pass filter is applied to the data. (a) Raw data. (b) Numerical interpolation of the raw data of 18 diodes.

the nature of the modes. The time delay observed between different lines-of-sight is caused by the poloidal rotation of perturbations. The spatiotemporal evolution of the perturbation amplitude measured by the XMCTS camera 1D is shown in figure 3 for a time interval of 400 μ s at $t = 3.4237$ s. The measured, bandpass-filtered perturbation amplitude (the same bandpass parameters as in figure 2(b)) is color-coded. Along the vertical axis the line-integrated data from the diodes in the camera 1D are plotted against the time on the horizontal axis.

4. Forward modeling of mode perturbations aligned on the magnetic flux surfaces

In order to extract information about the mode numbers and rotation direction from the line integrated SXR measurement we use a simplified eigenmode model for the mode pattern in the poloidal plane of the location of the SXR cameras (cf figure 4). It is possible to perform ‘virtual measurement’ along the lines-of-sight across the modeled x-ray radiation distribution. This ‘virtual measurement’ is performed via the

numerical integration for a given SXR camera geometry and using the flux surfaces from the plasma equilibrium calculated by VMEC. The expected signals for a radiation distribution can be modeled by the numerical integration and compared with the measured signals.

Figure 4 represents, as an example, a modeled $m = 10$ mode structure (color coded). The mode maxima and minima (blue color), consist of 2D Gaussians with their centers poloidally aligned on one of the magnetic flux surface. In this model, the constant background radiation distribution is assumed as subtracted, therefore, the negative radiation intensities can exist in the model. The individual 2D perturbation profile is modeled by the Gaussian $\xi_i = \xi_{0i} \cdot e^{-(\vec{r}-\vec{r}_i)^2/\sigma^2}$ where $\vec{r}_i = \vec{r}_i(t)$ is the coordinate of the perturbation center for a time point t , σ is the weight coefficient determining the spatial perturbation size and the index $i = 1, \dots, m$ indicates the perturbation number. Several attributes define the radiation distribution pattern: the number of maxima and minima (mode number m), the rotation velocity direction, the width of the Gaussians and their amplitudes (for a ballooning mode, the amplitude of the Gaussians varies with R and is maximal at the unfavorable curvature location). Using this approach a simultaneous presence of more

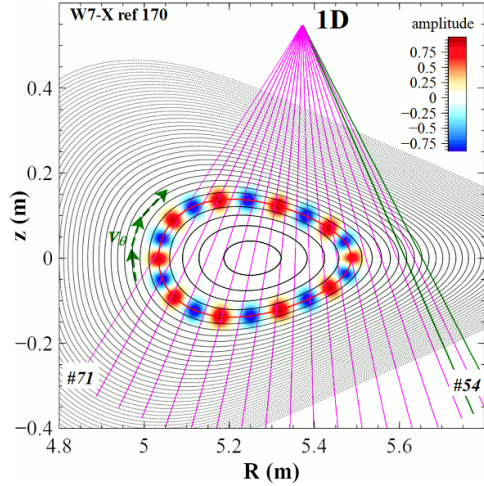


Figure 4. Lines-of-sight of the SXR camera 1D (magenta) across the magnetic flux surfaces are shown in black from VMEC (vacuum-field matching conditions of XP20 180 918.045). A model radiation distribution of 20 Gaussian-shaped perturbations (of alternating positive and negative amplitudes, $\sigma = 0.025$ m, color coded), exemplarily representing an $m = 10$ MHD mode located at $\rho \approx 0.3$ and poloidally propagating toward the green arrows. An SXR viewing angle of a single channel of 3.7° is marked in channel #54 (green).

than a single mode can be modeled. A similar signal processing approach for the SXR camera data has been reported by Weller *et al* for W7-AS [7] and used in ASDEX-Upgrade [9, 10]. The presented forward modeling of the mode structure is similar to that of [12, 13].

5. Determination of the radial location, poloidal mode numbers, mode rotation direction and mode type

5.1. Basic description of the method

The radial location of plasma modes can be estimated from the oscillation pattern shown in figure 2 as explained in the following. The oscillations are observed only by the SXR lines-of-sight which are crossing the modes. The edges of the rms distributions, where the mode amplitudes become observable, mark these radial locations. The radial mode locations are roughly equal to the impact parameters of these SXR lines-of-sight [7–11]. The phase evolution of the oscillations provides more detailed information about the mode dynamics. In our model description, one poloidal mode pattern is composed by a set of perturbations. Each of perturbations causes a relative increase (or decrease in the case of negative perturbations) of the measured SXR radiation along the corresponding line-of-sight. Due to the poloidal rotation of the mode structure along the flux surface, the time lags can be observed between those lines-of-sight which observe the plasma at different poloidal positions. For the following analysis the model described in section 3 is applied.

As a first step the radially thin perturbations ($\sigma = 0.001$ m) are used to fit the experimentally observed paths of centers

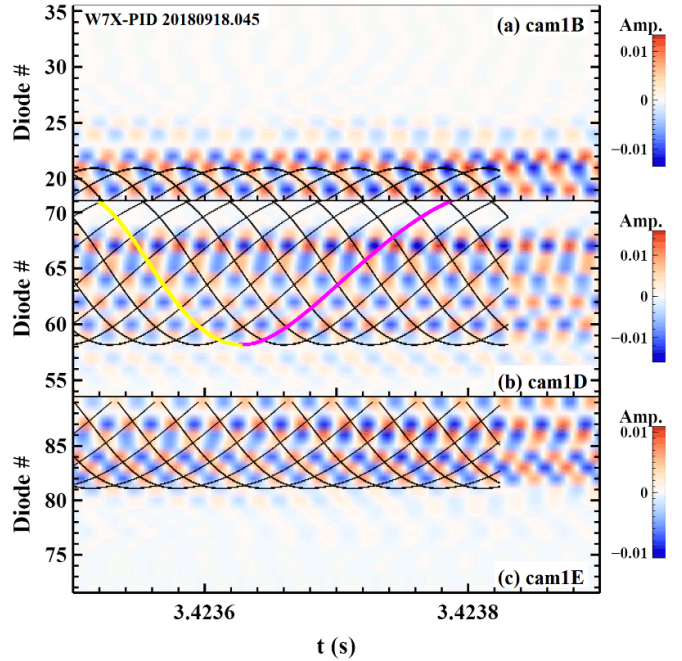


Figure 5. Evolution of an oscillating part of the experimental SXR emission measured by cameras 1B (top), 1D (middle) and 1E (bottom (color-coded)). The same 29–37 kHz band-pass filter, as in figure 3, is applied to the experimental data. The black lines mark the projected mode paths calculated for the maxima of a radially narrow $m = 10$ mode ($\sigma = 0.001$ m) in the case a single clockwise turn. For one of the selected maxima, the projected propagation is detailed for the movement near (yellow color) and far (magenta color) from the camera 1D.

of the perturbations by variation of the mode number. The paths of ten perturbations (i.e. mode maxima) are represented in figure 5 by the black lines. The width of the black lines represents a perturbation size of sigma ($\sigma = 0.001$ m) and the paths are plotted along 200 synthetic SXR channels to obtain a higher resolution. The experimental data are shown as a contour plot. Numerical interpolation of measured data is used in order to construct the SXR distribution along the cross-section on the base of 18 lines-of-sight.

The mode rotation in the poloidal direction is visible by the spatial shift of the perturbation with increasing time. A simultaneous rotation of the perturbations is observed by all operational XMCTS cameras, in particular 1B, 1D and 1E (as it is seen from figures 3 and 5). The perturbations cross the lines-of-sight twice during a full poloidal turn along the flux surface (see figure 4). The line-integration of the opposite propagating mode perturbations leads to the interference that causes the rather complex phase diagrams depicted in figures 3 and 5. The poloidal movement of individual perturbations projected onto the detection plane of the camera leads to an apparent propagation in the opposite directions for perturbations near and far with respect to the camera. In figure 5 the two directions are indicated by the yellow and magenta lines. The path along the distant part of the flux surface (magenta) is longer due to the divergence of lines-of-sight (cf figure 4) resulting in a lower projected velocity in the phase diagram. Here we assume the same poloidal linear velocity of the mode in the

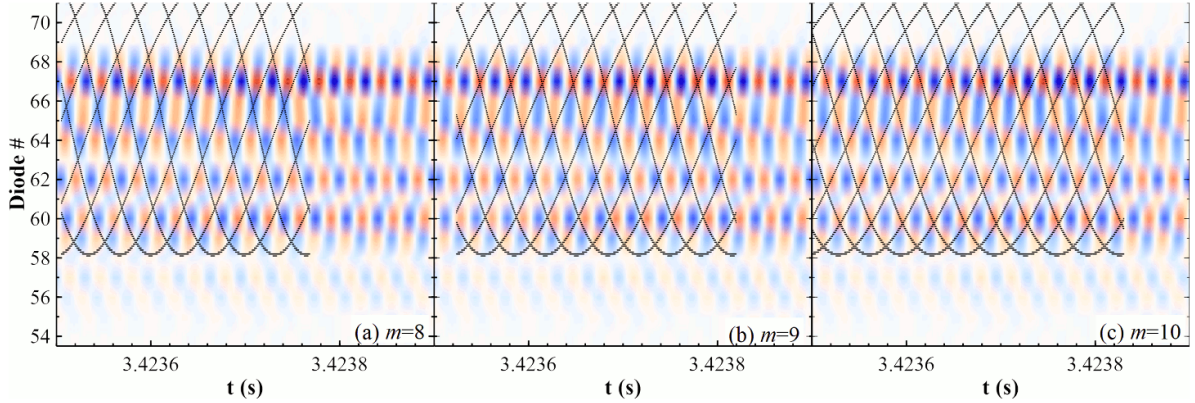


Figure 6. Evolution of an oscillating part of the experimental SXR emission measured by camera 1D (as in figure 5(b), the same for all the windows) and the numerical calculations of the $m = 8$, $m = 9$ and $m = 10$ mode paths (black lines) calculated for a radial narrow mode ($\sigma = 0.001$ m) for a single turn in the clockwise direction. The color-coding is the same as in figure 5.

near and far parts of the flux surface with respect to the camera. The different projected velocities enable us to determine the poloidal direction of mode rotation. From figure 5 one can deduce that the mode rotates in the clockwise direction [13]. The difference in the projection velocities can also be caused by asymmetry of the flux surfaces [12], but it is not a case of W7-X. Relatively sharp edges of the oscillation localizations in the space are visible in figures 2, 3 and 5. The oscillation amplitudes increase distinctly at channel #23 of camera 1B, at channel #58 of camera 1D, and at channel #81 of camera 1E. The impact parameters of these lines-of-sight correspond consistently to a normalized radius of $\rho \approx 0.3$. Note that for determining the radial location and the rotation direction of the mode, the model of figure 4 is not necessary as these parameters can be directly deduced from the (bandpass-filtered) raw data. Forward modeling is described for a detailed mode analysis. The poloidal mode number and radial mode location in the forward model are manually adjusted. In our calculations the case of a constant angular poloidal rotation velocity in the VMEC straight-line coordinate system [16] is used except especially mentioned cases. The path along the flux surface is used in our calculations for the poloidal mode velocity modeling. The distance between the neighboring points of the flux surface is passed during the uniform time interval in our model. For example, in the case of a constant linear mode velocity this distance is constant. We use the normalized path l_n in our calculations. The $l_n = 1$ value corresponds to the single poloidal turn of the mode. In order to compare these calculations with experimental data we perform the matching of two parameters: the initial phase and the rotation velocity. We adjust the phase by aligning the first crossing of the calculated perturbation paths with the maxima of the experimental perturbations. In the second step, we superpose other maxima of the experimental perturbations with another crossing in order to match the proportionality between time and l_n . By this step we adjust the poloidal rotational velocity. The matching of these two parameters should result in an agreement between the experimental data and calculated mode paths, if the poloidal mode number m and the radial location ρ are matching. A comparison of the calculated mode paths for

different mode numbers with the experimental data is shown in figure 6.

The maxima of the experimental data coincide only with the modeled mode paths (black lines) for the $m = 10$ mode (figure 6(c)). The low amplitudes of the mode traces for channels #69–71 of camera 1D are caused by the decreased signal intensity due to the partly shadowed photodiodes (further details can be found in [5]). Figure 7 shows the effect of the radial mode perturbation width. A modeled $m = 10$ mode having a wider perturbation size ($\sigma = 0.025$ m) is compared with the experimental data. The effect of the finite perturbation width, causing oscillations in channels #56 and #57 of camera 1D, is in good agreement with the experimentally measured data.

5.2. Comparison of various poloidal velocities

Two equivalent approaches can be used for modeling the variable mode velocity, as it was highlighted in the introduction. A spatiotemporal analysis is used to model the phase dynamics of line-integrated oscillations mentioned in the foregoing chapter. It is logical to determine the phase mode velocity v_Φ (equal to the perturbation velocity) directly, in contrast to an implicit definition by the spatiotemporal analysis based on the wavevector. It is possible to use the poloidal angle θ of the perturbation or the perturbation position at the magnetic surface l for the poloidal dependence modeling. In our modeling we use the perturbation position normalized to the magnetic surface perimeter length l_n . The linear phase velocity is $v_\Phi = dl/dt \approx \Delta l/\Delta t$. It is matched with the experimental one via the scaling, as described above. Thus we can use a variable perturbation step Δl along the magnetic flux surface for a uniform time interval Δt as a gauge of the variable phase velocity. An actual experimental phase velocity is compared with the modeled one by the implicit Δt selection. Also we use the dependence of this step on the magnetic surface position $\Delta l(l)$ or $\Delta l(l_n)$.

The poloidal phase mode velocity depends on the driving instability as well as on the plasma rotation velocity. In turn, the poloidal phase velocity depends on the ρ value and

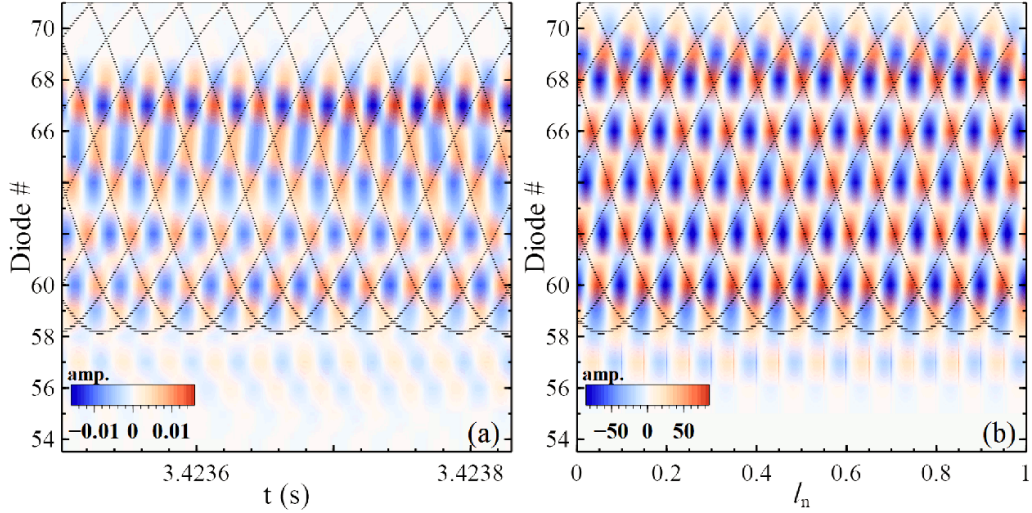


Figure 7. Evolution of (a) experimental and (b) modeled data of the $m = 10$ mode (mode size $\sigma = 0.025$ m). The same numerical interpolation of the 18 channels is used for both graphs. The black lines indicate the $m = 10$ mode path calculated for a thin mode ($\sigma = 0.001$ m) for a single clockwise turn.

poloidal angle θ . However, a detailed analysis of the plasma background physics [14, 15] is outside of the scope of the present work. Below we compare three different cases of the mode rotation to demonstrate once more the forward modeling technique. The case of a constant angular poloidal phase velocity in the VMEC straight-field-line coordinate system is the reference one. This case is used in all the calculations represented above. It is compared with the case of a constant angular poloidal phase velocity in the physical coordinate system and with the case of a constant linear phase velocity. The angular dependence of the phase velocity is modeled via different distances between the neighboring points on the flux surface. The mode passes these distances during the uniform time interval. In our model the neighboring points on the flux surface are chosen by the $u = \text{const}$, $\theta = \text{const}$ or $l = \text{const}$ laws, where u is the poloidal coordinate in the VMEC straight-field-line coordinate system [16], θ is the physical poloidal angle and l is the path along the flux surface. The comparison of these calculations is shown in figure 8 for the case of thin perturbations ($\sigma = 0.001$ m).

The two cases: $u = \text{const}$ and $l = \text{const}$ are in a good agreement with the experimental data (cf figure 8). The dependence of the mode rotation velocity on the poloidal angle introduces an additional correction to the calculated phase diagram of the modes, but the main features are defined by m and ρ of the mode.

Modeling of the thick perturbations can introduce one more correction to the phase diagram of the modes. The shape of perturbations can be flexible. The perturbation size along the magnetic flux surface and in the perpendicular direction can depend on the poloidal angle. This flexibility can be explained by the angular dependence of the mode wave vector and, consequently, of the phase velocity perturbation. The perturbation size parallel to the flux surface is increasing in the regions of a higher phase velocity. The size of the perturbation in the perpendicular direction can depend on the set of factors such

as a size of the perturbation in the parallel direction, such as a distance between the neighboring flux surfaces. The perturbation shape should be constructed by the curvilinear shape of the flux surface. This curvature can be neglected in the case of the high m -modes under consideration. In this case the displacement of the flux surface from the straight line in the small enough length of perturbation is rather insignificant. We can use a rotating Cartesian coordinate system (x, y) with the axis x parallel to the flux surface and the axis y perpendicular to the flux surface for every position in the flux surface l . The individual 2D perturbation profile in this case is modeled by the Gaussians $\xi_i = \xi_{i0} \cdot e^{-(x-x_i)^2/\sigma_x^2(l)} \cdot e^{-(y-y_i)^2/\sigma_y^2(l)}$ where x_i and y_i are the coordinates of the perturbation center for the position along the flux surface l ; σ_x and σ_y are the corresponding weight coefficients. We cannot simulate a real plasma mode without knowledge of $\sigma_x(l)$ and $\sigma_y(l)$ dependences in this mode. Nonetheless, according to our simulation, the distortions of the phase diagram are not significant even in the case of the strong $\sigma_x(l)$ and $\sigma_y(l)$ dependences. The comparison of a rigid mode case with a flexible perturbations case possessing a strong flexibility: $\sigma_x \sim \Delta l^2$, $\sigma_y \sim \Delta l^{-1}$ is shown in figure 9.

The phase diagrams are rather similar in the two models as is seen from figures 9(c) and (d). This effect has been expected in the high- m case under consideration. The phase diagram is determined mainly by the centers of the short in comparison with the flux surface length perturbations.

5.3. Ballooning-like mode analysis

We use the modes with a single poloidal mode number, although the modes with co-existing different poloidal mode numbers could be observed by XMCTS. For modeling of a ballooning-like mode we use the sum of perturbations of two modes with poloidal mode numbers $m = 10$ and $m + 1 = 11$ with equal radial location and size ($\sigma = 0.025$ m). In figure 10

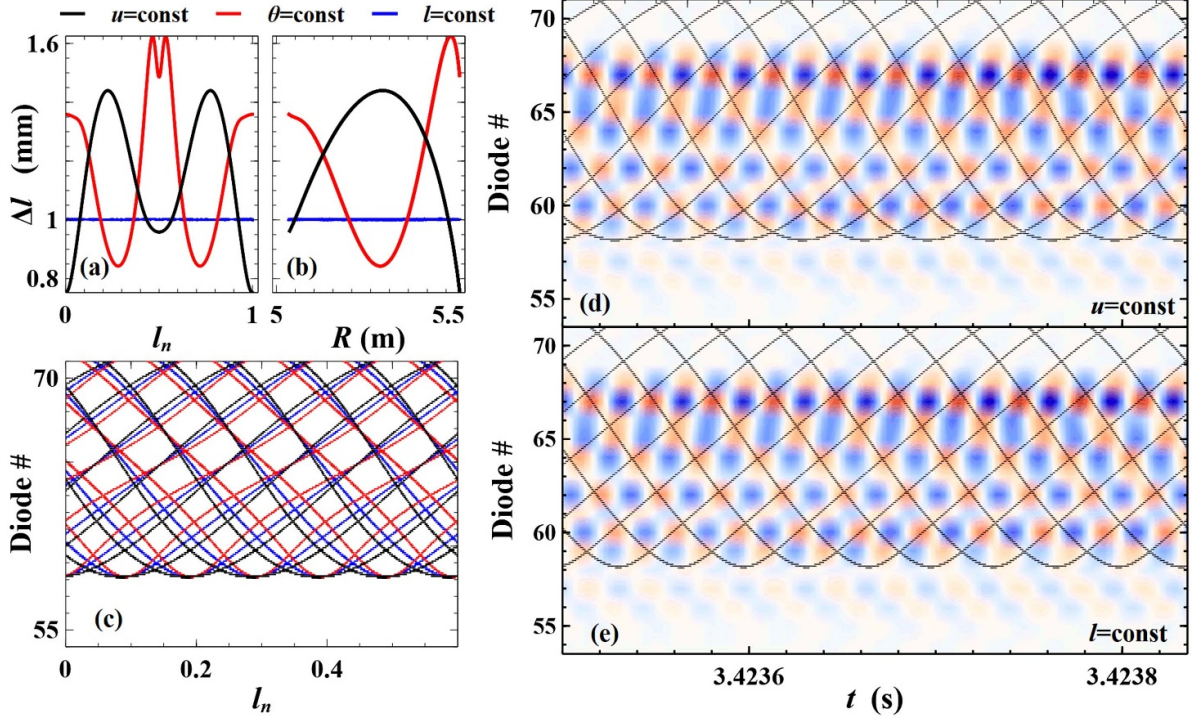


Figure 8. Step Δl versus the position on the flux surface (a) and the major radius (b) for the constant VMEC velocity, constant angular velocity and constant linear velocity modeling; (c) lines mark $m = 10$ ($\sigma = 0.001$ m) mode paths calculated for the three phase velocities (marked by the same colors); (d), (e) camera 1D experimental data and $m = 10$ ($\sigma = 0.001$ m) mode paths as black lines for $u = const$ and $l = const$ respectively.

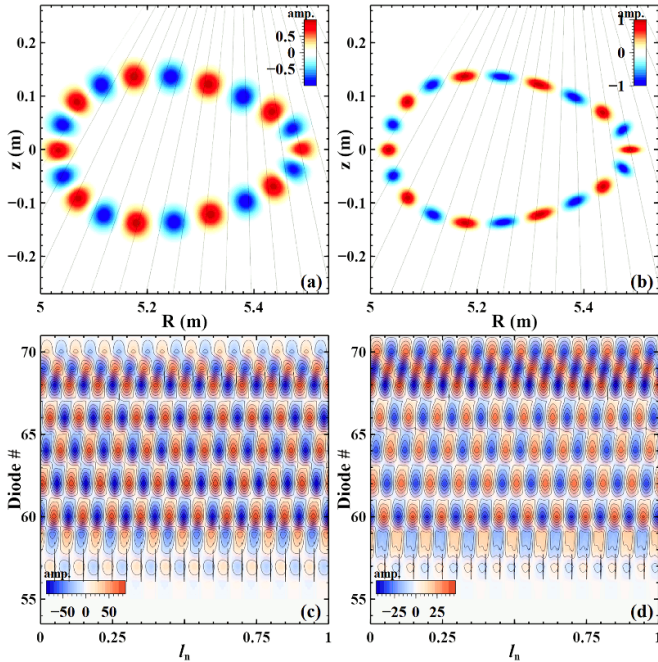


Figure 9. Modeled topology of the $m = 10$ mode: (a) rigid model ($\sigma = 0.025$ m) and (b) flexible model. The corresponding evolution of the modeled line-integrated responses (c) and (d).

the non-ballooning $m = 10$ mode is compared with the $m = 10$ ballooning-like mode. A stable pattern of the SXR response is formed in the single m case (figure 10(c)) in contrast to the time-varying SXR response of the ballooning-like mode

(figure 10(d)). An interference of perturbations of m and $m + 1$ modes causes a distortion of the SXR response pattern. Similar distortions are observed in the case of the anti-ballooning mode or in the cases of combination of m and $m + 2$ modes (typical for the ellipticity induced by the Alfvén eigenmodes, EAE). If the amplitude of one of the poloidal harmonics of the combined mode is substantially higher, this mode is seen as a single m mode. A regular, stable pattern of the SXR response is observed experimentally at 3.42 s (as seen from figures 3, 5 and 7(a)). We can conclude that the observed mode is determined as an $m = 10$ single poloidal mode (or a mode with the strongly dominant $m = 10$ component).

5.4. Amplitude distribution analysis

One more available experimental property of the modes under consideration is the time-averaged mode amplitude distribution (see figure 2). It is expected that the perturbation interference in the case of multiple m modes should form different patterns of the time-averaged mode amplitude. Non-uniformity of the fluctuations amplitude are observed in figure 2(b) and (c) at 3.3–3.4 s but are not observed in figure 2(c) at 3.5 s. Figure 11 shows the amplitude distribution versus the photodiode obtained by numerical integration of the data given in figures 10(c) and (d) for single m mode and ballooning-like modes.

The time-averaged amplitude distribution is clearly different, as it has been expected. A more uniform distribution in the case of ballooning-like modes (and other multiple m modes)

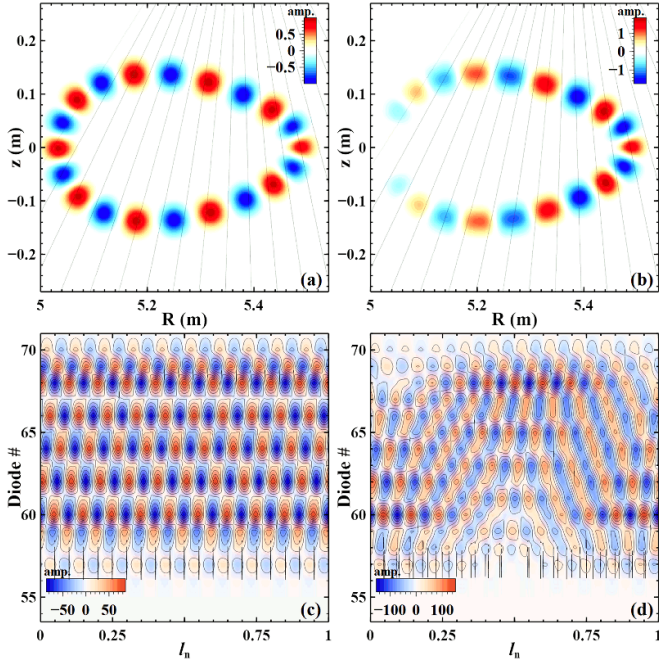


Figure 10. Modeled topology of (a) an $m = 10$ mode and (b) an $m = 10$ ballooning-like mode ($\sigma = 0.025$ m). The corresponding evolution of the modeled line-integrated responses (c) and (d).

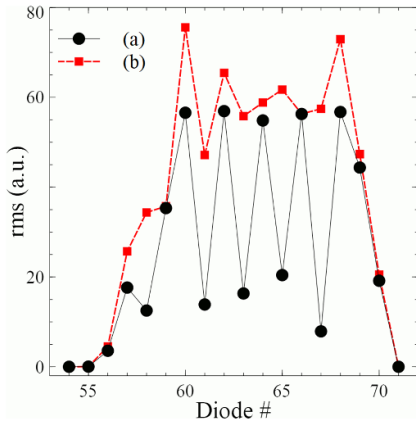


Figure 11. Distribution of rms amplitudes of the modeled mode structure: (a) for a single m mode, as in figure 10(c), and (b) for a modeled ballooning mode, as in figure 10(d). The rms values of oscillations are plotted versus photodiodes of camera 1D.

is substantially different from the uniform case of a single m mode. Thus, our numerical modeling shows not only a similar phase evolution of the perturbations but also demonstrates a non-uniform distribution of the experimentally observed fluctuation amplitudes (see figure 2) in the case of a single m mode. This non-uniform distribution is used for discrimination of single m modes from other modes. Three branches of W7X-PID 20180918.045 contain the non-uniform distribution of the SXR oscillations amplitude as is seen from figure 2. The branch observed at 3.5 s contains a rather uniform distribution. This last branch is caused by the multiple- m

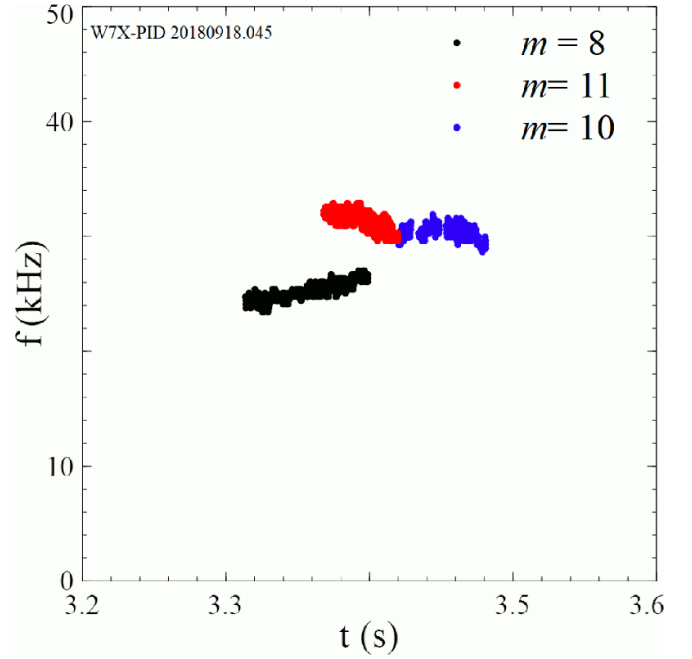


Figure 12. Poloidal mode numbers of the three different mode branches in the discharge W7X-PID 20180918.045 (raw FFT spectra shown in figure 2(a)).

mode according to the criterion of the amplitude distribution uniformity.

5.5. Mode numbers in the W7X-PID 20180918.045 discharge

The capabilities of the forward modeling technique are demonstrated in the foregoing sections. The application of the described numerical forward modeling of mode structures to different parts of the spectra allows separating of three different single m mode branches in the W7-X discharge W7X-PID 20180918.045, as shown in figure 12.

The separation of the mode branches follows from the comparisons to the modeled oscillation phase analysis as well as directly from the mode amplitude distribution analysis of the raw data (as shown in figure 2). One can see from figure 2 that the last branch (23–28 kHz at 3.5 s) is a more complex case. The responsible mode cannot be described by a single poloidal mode number m . A more detailed analysis of the combined m case (discrimination from $(m, m + 1)$; $(m, m + 2)$; ... combinations) is limited by the spatial resolution of a single SXR camera. The combination of all the 20 available XMCTS cameras in W7-X and more complex modeling may provide a more sophisticated technique in this case. Our forward modeling technique can be used for determination of single m modes in the W7-X discharges. It can be used for discrimination of more complex mode structures from the single m modes as well. The dependence of mode rotation velocity on poloidal angle can introduce an additional correction to the calculated phase diagram of the modes, but the main features are defined by m and ρ of the mode.

6. Conclusions

A forward mode modeling technique of MHD mode analysis on the base of lines-of-sight data of SXR diagnostics is first applied for W7-X geometry. The real geometry of SXR cameras is used in our modeling. The poloidal mode structures are modeled by the radially localized Gaussian-shaped emission regions rotating along the magnetic surfaces. A set of models with a constant phase velocity and a phase velocity depending on the poloidal angle are considered. A model with rigid shapes of emission regions are compared with a flexible model of these regions. In this model the parallel and perpendicular sizes of the flexibly shaped emission regions depend on the poloidal angle. Two techniques based on the comparison of calculated and measured data are used. The calculated spatiotemporal phase evolution of line-integrated modeled data is compared with the experimental data in the first technique. The spatial distribution of the oscillation amplitudes versus the SXR channel is compared in the second technique. All the models shows, that in the case of a high- m mode the phase diagram is determined mainly by the poloidal mode number m and radial location of mode ρ . So, this technique allows us to determine reliably the radial location ρ , poloidal mode number m and mode rotation direction of high- m modes with a single m . Thus the single m modes are discriminated from other modes (for example, ballooning modes). In particular, in the discharge #180918045 there are identified three single m mode branches with poloidal mode numbers $m = 8$, $m = 10$, $m = 11$ localized at $\rho \approx 0.3$ and rotating in the clockwise direction (when looking in the positive toroidal direction). As a result, using the forward modeling in W7-X the high m -modes are identified.

Data availability statement

The data that support the findings of this study are available upon reasonable request from the authors.

Acknowledgments

This work has been carried out within the framework of the EUROfusion Consortium and has received funding from the Euratom research and training programme 2014–2018 and

2019–2020 under Grant Agreement No. 633053. The views and opinions expressed herein do not necessarily reflect those of the European Commission.

ORCID iDs

M B Dreval [ID](https://orcid.org/0000-0003-0482-0981) <https://orcid.org/0000-0003-0482-0981>
C Brandt [ID](https://orcid.org/0000-0002-5455-4629) <https://orcid.org/0000-0002-5455-4629>
J Schilling [ID](https://orcid.org/0000-0002-6363-6554) <https://orcid.org/0000-0002-6363-6554>
H Thomsen [ID](https://orcid.org/0000-0002-6835-1494) <https://orcid.org/0000-0002-6835-1494>
A Beletskii [ID](https://orcid.org/0000-0003-3320-9604) <https://orcid.org/0000-0003-3320-9604>

References

- [1] Nührenberg C 1999 *Phys. Plasmas* **6** 137
- [2] Rahbarnia K *et al* 2018 *Nucl. Fusion* **58** 096010
- [3] Edlund E M, Porkolab M, Huang Z, Grulke O, Böttger L-G, Von Sehren C and Von Stechow A 2018 *Rev. Sci. Instrum.* **89** 10E105
- [4] Thomsen H *et al* 2013 *Proc. 40th EPS Conf. on Plasma Physics* P2.011 (<http://ocs.ciemat.es/EPS2013PAP/pdf/P2.011.pdf>)
- [5] Brandt C, Broszat T, Thomsen H, Laube R, Marquardt M, Franz P, Schülke M, Sieber T and Weißflog S 2017 *Fusion Eng. Des.* **123** 887
- [6] Brandt C *et al* 2020 *Plasma Phys. Control. Fusion* **62** 035010
- [7] Weller A *et al* 2007 *Proc. 34th EPS Conf. on Plasma Physics* P1.112 (http://epsppd.epfl.ch/Warsaw/pdf/P1_112.pdf)
- [8] Razumova K A *et al* 2003 *Plasma Phys. Control. Fusion* **45** 1247
- [9] Igochine V, Günter S and Maraschek M The ASDEX Upgrade Team 2003 *Nucl. Fusion* **43** 1801
- [10] Weiland M, Gude A, Igochine V, Maraschek M, Zohm H, Bohle R, Dux R, Lackner K, Odstrčil T and Pütterich T 2015 *Plasma Phys. Control. Fusion* **57** 085002
- [11] Franz P, Marrelli L, Piovesan P, Chapman B E, Martin P, Predebon I, Spizzo G, White R B and Xiao C 2004 *Phys. Rev. Lett.* **92** 125001
- [12] Dreval M B, Shapoval A M, Ozherelyev F I and Makhov M M 2016 *Rev. Sci. Instrum.* **87** 073503
- [13] Dreval M, Xiao C, Elgriw S, Trembach D, Wolfe S and Hirose A 2011 *Rev. Sci. Instrum.* **82** 053503
- [14] Edlund E M, Porkolab M, Kramer G J, Lin L, Lin Y and Wukitch S J 2009 *Phys. Rev. Lett.* **102** 165003
- [15] Heidbrink W W 2008 *Phys. Plasmas* **15** 055501
- [16] Hirshman S P and Whitson J C 1983 *Phys. Fluids* **26** 3553